

Neural network biased corrections: Cautionary study in background corrections for quenched jets

D. Stewart and J. Putschke
Wayne State University, Detroit, Michigan 48201
(Dated: December 23, 2024)

Jets clustered from heavy ion collision measurements combine a dense background of particles with those actually resulting from a hard partonic scattering. The background contribution to jet transverse momentum (p_T) may be corrected by subtracting the collision average background; however, the background inhomogeneity limits the resolution of this correction. Many recent studies have embedded jets into heavy ion backgrounds and demonstrated a markedly improved background correction is achievable by using neural networks (NNs) trained with aspects of jet substructure which are used to map measured jet p_T to the embedded truth jet p_T . However, jet quenching in heavy ion collisions modifies jet substructure, and correspondingly biases the NNs' background corrections. This study investigates those biases by using simulations of jet quenching in central Au+Au collisions at $\sqrt{s_{NN}} = 200$ GeV with hydrodynamically modeled quark-gluon plasma (QGP) evolution. To demonstrate the magnitude of the effect of such biases in measurement, a leading jet nuclear modification factor (R_{AA}) is calculated and reported using the NN background correction on jets quenched utilizing a brick of QGP.

I. INTRODUCTION

Heavy ion collisions at ultra-relativistic speeds were first proposed to provide the experimental conditions necessary to create and study the quark-gluon plasma (QGP), a novel phase of matter predicted by the completion of the standard model of physics in which quarks and gluons are deconfined throughout an extended volume [1]. Correspondingly, QGP signals were observed with the first data from collisions at the Relativistic Heavy Ion Collider (RHIC) [2–5] and then the Large Hadron Collider (LHC) [6–8]. The study of QGP formation, properties, evolution, and hadronization, has remained the central motivation of ultra-relativistic heavy ion collision research for the past quarter century. The reader is referred to [9] for a recent overview.

Rare, high- Q^2 scattered partons, jets, in ultra-relativistic heavy-ion collisions occur early in the collision evolution. Therefore, they provide intrinsic colored probes which undergo scattering and induced gluon emission, i.e., jet quenching, while traversing the QGP, which is a hot, dense, colored medium. The simplest experimental proxy for these initial hard partons are high transverse momentum (p_T) hadrons, and indeed one of the first strong evidences for QGP formation, predicted in 1982 by J. D. Bjorken (see [10]), was the disappearance (quenching) of high- p_T hadrons in central (i.e., head-on) Au+Au collisions at RHIC in 2004 [11].

In subsequent years, infrared-safe and collinear-safe clustering algorithms [12] have been used to combine clusters of collimated particles into aggregate objects called jets. Jets provide many advantages over individual hadrons, not least of which is they provide a better proxy for the initial scattered parton with more of the originating p_T recaptured experimentally. However, they are also complex objects collecting all measured particles within a physical geometric acceptance, generally measured in

coordinates of pseudo-rapidity (η) and azimuth (ϕ). In heavy ion collisions this collection includes many “background particles”: particles not originating from the initiating partonic hard-scattering, but rather from many of the other participating colliding nuclei or even additional (soft) scatterings of the originating hard-scattered partons. For a recent overview of jet measurements see [13].

At RHIC, jets have been measured up to around 40 GeV/c [14–16]. For comparison, in the 5% most central collisions of Au+Au ions at $\sqrt{s_{NN}} = 200$ GeV, the background particles contribute, on average, around 45 GeV/c of additional p_T to anti- k_T jets with $R = 0.4$, where R is the jet resolution parameter and is approximately equal to the jet radius in $\eta \times \phi$ space [17].

The area-based (AB) method is a common experimental procedure to correct for the heavy background. Proposed in 2007 [18], and later implemented by the authors in the FastJet package [19], this method measures the median background density (ρ_{bkg}) in each event and then corrects the p_T of measured jets ($p_{T,\text{jet}}^{\text{reco}}$) by ρ_{bkg} scaled by the jet area: $p_{T,\text{jet}}^{\text{corr}} \equiv p_{T,\text{jet}}^{\text{reco}} - \rho_{\text{bkg}} A_{\text{jet}}$. The jet areas (A_{jet}) for anti- k_T jets are relatively stable [17] and therefore have little impact on the AB correction, and the effect of the leading p_T jets on ρ_{bkg} is algorithmically minimized by disregarding the one or two highest p_T jets while calculating ρ_{bkg} . As a result, the AB method's corrections utilize principally information from the event background, and is therefore insensitive to jet substructure.

The resolution of the AB method, parametrized in this paper by the distribution of the residual errors between the corrected jet p_T and the actual truth jet p_T ($\delta p_{T,\text{jet}} \equiv p_{T,\text{jet}}^{\text{corr}} - p_{T,\text{jet}}^{\text{truth}}$), is dominated by region-to-region fluctuations in the background densities. In experiment, these must be corrected statistically, typically at the same time as the jet energy spectra and resolution

due to detector effects. These are on the order of 8 GeV/c per $R = 0.4$ jet in central Au+Au collisions at RHIC and are the principle limitation on jet measurement resolution in these heavy-ion collisions. Alternatively, at kinematics achievable in collisions at the LHC, jets are available at much higher values of p_T , but the lower-boundary of p_T available to jet measurements is also limited by the resolution of the background fluctuations.

In order to improve the resolution of jet measurements beyond the fundamental limitation imposed by background fluctuations, additional information is needed. More than 40 years of development incorporating both perturbative calculations and models for fragmentation and hadronization have yielded well-tuned Monte Carlo simulators for high-energy pp collisions [20–22]. It is natural to take the jet parameters of these pp simulations and see if some combination of observable signals from jet substructure can be combined with the ρ_{bkg} , $p_{T,\text{jet}}^{\text{reco}}$, and A_{jet} of the AB method, to improve the jet p_T background subtraction in heavy-ion collisions. This search is facilitated by the powerful tools afforded by Machine Learning (ML), which can learn and apply correlations of essentially arbitrary dimensionality. Indeed, it has been demonstrated in prior publications (and reconfirmed in this present paper) that neural networks (NNs) gain significant discriminatory power in correcting jets for background fluctuations if they are provided the p_T values of the leading jet constituents or even just the total number of jet constituents [23–25].

A principle motivation to study jet p_T in heavy ion collisions is to measure quenching, in which the jet substructure is modified through partonic energy interactions with the QGP. Consequently, there is significant uncertainty about substructure in quenched jets relative to that in vacuum jets. This relative uncertainty propagates in any calculation dependent on jet substructure, e.g., specific detector response effects, and is also present in selections of rare- pp collisions, such as those resulting in ultra-high particle multiplicities. The difficulties posed by using jet substructure to correct for heavy backgrounds to measure jet quenching are particularly problematic: the partonic energy loss modifies the jet substructure, and a particular jet substructure must be assumed for the background correction to measure quenching. Inaccuracy in the assumed substructure introduces a bias in the background p_T correction. This paper investigates those biases by using NNs trained on pp jets and using them to background correct quenched jets. In order to indicate how such a bias may propagate in actual jet measurements, it also reports an error of a simulated measurement of the nuclear modification factor R_{AA} of a quenched jet spectrum.

A measurement of R_{AA} using both area-based and ML-based background corrections been published for collisions at LHC in [24] in which the ML-based measurements have significantly higher systematic errors but reach lower jet p_T values than previously accessible using the area-based method. This current paper is com-

plementary in the sense that it investigates the effects in collisions at RHIC energies, with its associated steeper jet p_T spectrum and different background conditions.

This study utilizes the JETSCAPE framework [26] to generate jets in both pp collisions and central Au+Au collisions at $\sqrt{s_{NN}} = 200$ GeV, using tune parameters from [27, 28]. The Au+Au collision simulations hydrodynamically model the QGP production and evolution and are hereafter referred to as “hydro events” in this study. This collision system and energy has been selected to match the collisions scheduled for RHIC’s 2025 run. The simulations in these hydro events is the best available to use with jet quenching Monte Carlos (MCs), and this is the first study to use them to investigate ML. They do not, however, model medium response to the jets. The hydro events also provide realistic hadron backgrounds for central Au+Au events. In all cases, for the pp and heavy ion events, the particles are used as-provided by the Monte-Carlo, without any additional simulation to account for detector effects or efficiencies.

Using the jets from the pp events along with the backgrounds from the hydro events, we train NNs and reconfirm the findings from previous studies (e.g., [23, 25]) which show the ability of NNs to p_T correct jets for heavy ion backgrounds – using both charged and neutral particles – from the hydro events, clustering the combined events, and geometrically matching the resulting jets to the pp jets clustered in vacuum. We train NNs to map the matched composite jets to the vacuum jets using various selections of jet parameters. The goodness of the resulting correction is defined by the distributions of the p_T residual errors, $\delta p_{T,\text{jet}}$.

While they are the best option for jet quenching simulations, the hydro events are also very computationally expensive. In order to generate a full spectrum of quenched jets, we also used jets simulated by quenching in fixed-length “bricks” of QGP. These are much faster to generate and allowed the generation of the several million jets which compose the full spectrum. These were generated in order to provide a standard jet quenching measurement, an R_{AA} , in order to discuss the biases.

We report the jet quenching via the modification of the jet fragmentation in the hydro and in brick events using brick lengths up to six fm. We also report the $\delta p_{T,\text{jet}}$ distributions for the NN background corrections for these jets. To do this, the brick jets were embedded into backgrounds from the hydro events. This creates reasonable, computationally-cheap, approximation of a hydro event; however, it also destroys effects from variable path lengths and the evolving medium on jet quenching. These $\delta p_{T,\text{jet}}$ distribution studies serve two purposes. First, they measure the progression of biases in $\delta p_{T,\text{jet}}$ with increasing amounts of quenching. Second, they determine the brick length whose quenching is most equivalent to the quenching in hydro events. That brick length is then used for a full-spectrum of quenched jets.

Finally, to demonstrate the magnitude of the effect on

final jet measurements that can result from the propagation of the $\delta p_{T,\text{jet}}$ biases, we simulate an R_{AA} measurement for the leading, i.e. highest- p_T , jet per event. In this simulation, the “data” consists of the full spectrum of jets quenched in QGP bricks and embedded into hydro backgrounds. The measured jets are background corrected using the NNs, which were trained on pp jets embedded in the hydro backgrounds. Using the same algorithm as used in experimental measurements, the process inefficiencies are corrected on an ensemble level to a final “measured” p_T spectrum. The ratio of this spectrum to the vacuum pp spectrum (R_{AA}^{LeadJet}) is presented and compared to the actual R_{AA}^{LeadJet} from the brick events.

II. DATA SIMULATION: PRODUCTION AND PROCESSING

Note: The libraries used are listed in Appendix B. The code and notebooks used are archived online at <https://github.com/davidstewart/jet.and.thermal>.

A. Jet Simulation

The JETSCAPE framework was used to simulate hard scatterings of initial partons, along with their subsequent evolution and hadronization. Jets were generated using the input Monte Carlo input parameter \hat{p}_T , which constrains the transverse momentum of the initiating partons (IP) in the hard scattering. (For illustration, refer to Fig. A.2 in the appendix, which shows the p_T distributions of jets resulting from different \hat{p}_T selections.) We generated groups of jets at both discrete \hat{p}_T values – which correspond to tightly clustered jet p_T – and from groups of events with a range of \hat{p}_T ’s, each weighted to account for the \hat{p}_T cross sections, in order to simulate continuous, steeply falling, unbiased p_T jet spectra.

JETSCAPE also simulated jet quenching in a QGP. A hydrodynamically simulated QGP was generated for 3100 Au+Au collisions with 0-5% centrality at $\sqrt{s_{NN}} = 200$ GeV. Each of these hydro events was hadronized 10 times and embedded with a unique jet each time, for a total of 31,000 jets quenched in hydro. Additionally, millions of quenched jet events were simulated using QGP bricks of various discrete thicknesses. A spectrum of pp (i.e., non-quenched) jets was generated both as a baseline, and as a dataset used to train the neural networks. Finally, an additional spectrum of jets quenched in QGP bricks of length 3.5 fm was generated.

The effects of jet quenching on the jet constituent particles’ p_T is shown in Fig. 1 for jets in $\hat{p}_T \in [30, 31]$ GeV/ c events. The figure shows the jet fragmentation function, the average number of constituents per jet in increments of “ Z ”, the fractional constituent p_T relative to the p_T of the IP (as opposed to lower-case “ z ”, in which the constituent p_T values are scaled by their fraction of the jet p_T instead of the IP p_T). The results show that the hy-

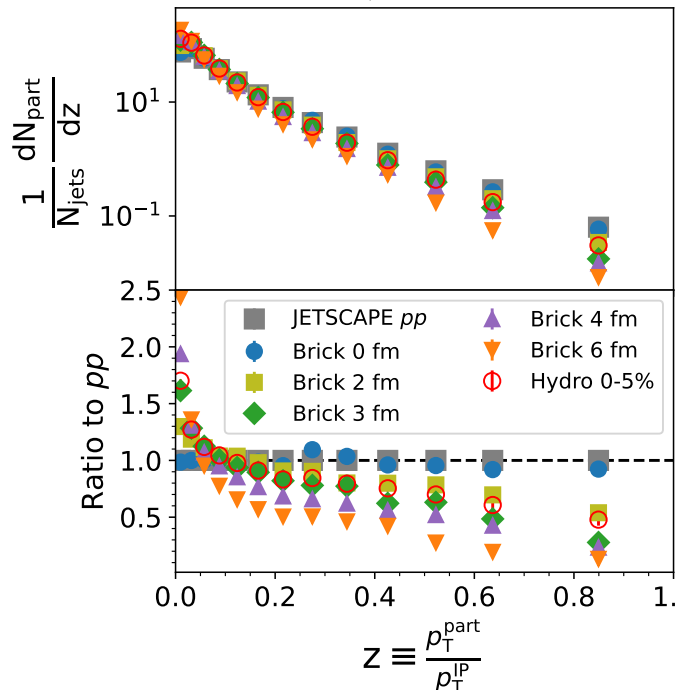


FIG. 1. Distribution of the number of jet constituents ordered by their p_T (p_T^{part}) scaled by the p_T of the initiating parton (p_T^{IP}) for events with $\hat{p}_T \in [30, 31]$ GeV/ c . Statistical error-bars are mostly smaller than marker sizes.

dro events have quenching effects at low Z comparable to QGP brick lengths of 3-4 fm, and at higher Z comparable to 2-3 fm.

B. Background Production

JETSCAPE identifies particles resulting from high- p_T scatterings from the background particles separately from those resulting from other processes. When clustered without the background particles, these result in “truth jets”; when clustered with background particles, they result in “reco-jets”. The hydro events generate realistic distributions of background particles, and therefore the set of background particles in each hydro event is saved into an external file. When processing the events with bricks of QGP (or without any QGP) only the particles of the leading truth jets are kept, while the background particles and other truth jets are discarded. The saved truth jet particles are embedded into a set of background particles from a hydro event before reconstructed as reco-jets.

The distribution of the number of background of particles per hydro event is given in Fig. 2; distributions in ϕ , η , and p_T are also given in the Appendix in Fig. A.1.

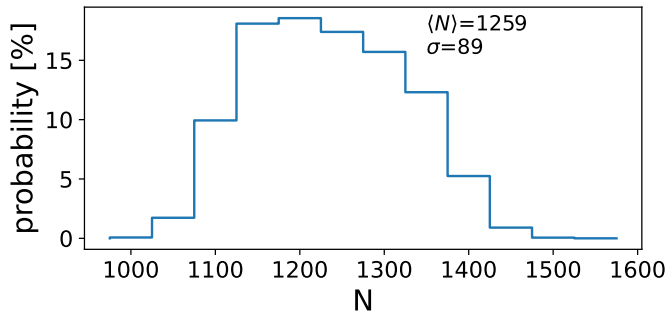


FIG. 2. Distribution of the numbers of background particles per event.

C. Jet Clustering and Matching

The input data for each event consists of the set of particles associated with only the highest p_T initiating parton, which are clustered into the truth jets, and the set of background particles generated from a hydro event. (For all jets generated in an hydro event, the jet is always clustered with the background particles from the same event). In each event, the following process was followed, utilizing FastJet [19] version 3.4.2 for all jet clustering with jet resolution parameter $R = 0.4$.

1. Use only the highest- p_T IP scattering for all hard scatterings in each event.
2. Cut events with IP pseudorapidity $\eta^{\text{IP}} > |1.0|$.
3. Cluster all final-state particles resulting from the selected IP into anti- k_T jets. Consider all jets relative to the IP within distance $(\Delta R \equiv \sqrt{(\eta^{\text{jet}} - \eta^{\text{IP}})^2 + (\phi^{\text{jet}} - \phi^{\text{IP}})^2})$ of $\Delta R < 0.4$. Discard the event if there are no such jets. If there are, select the highest- p_T of these jet as the truth jet with $p_{T,\text{jet}}^{\text{truth}}$.
4. Cluster the background particles into k_T jets [29]. In hydro events, use the background particles from the same hydro event in the clustering. In all other events, use the background particles saved from one of the hydro events.
5. Remove the two highest p_T jets, and record the median jet- p_T density ($p_{T,\text{jet}}/A_{\text{jet}}$) as ρ_{bkg} .
6. Cluster the jet constituents and the background particles together into anti- k_T jets. Select all resulting jets that are within $\Delta R < 0.3$ of the truth jet. If there are none, discard the event. Otherwise, the highest- p_T of these jets is the “reco jet” with $p_{T,\text{jet}}^{\text{reco}}$.
7. Record $p_{T,\text{jet}}^{\text{truth}}$, $p_{T,\text{jet}}^{\text{reco}}$, and other event parameters used to train Neural Networks. A list of which parameters are used to train each neural network is given in Table I.

TABLE I. Neural network (NN) training parameters

Label	Additional Training Parameters [†]
NN _{AB}	(none)
NN _{Ang}	Angularity: $\alpha \equiv \sum_i p_{T,i} \Delta R_i$, where i runs over all constituents, and ΔR_i is the η - ϕ distance from the constituent to the jet axis
NN _{Ncons}	The number of jet constituents
NN _{pTcons}	p_T of the highest- p_T constituents (limited to 10) in the reco jet
NN _{AllReco}	All parameters listed in this chart together

[†] $p_{T,\text{jet}}^{\text{truth}}$, $p_{T,\text{jet}}^{\text{reco}}$, A_{jet} , & ρ_{bkg} , are used with each NN

D. Neural Network Training

The NNs were trained using the TensorFlow library [30]. Each NN was composed of a sequential model using RELU activation functions with three dense layers of 100, 50 and 50 nodes respectively, with an additional final layer of a single node for the output value ($p_{T,\text{jet}}^{\text{truth}}$). Each NN was trained with 12 epochs.

In order to train the neural networks, an set of pp jets with a flat p_T spectrum was generated, clustered, and embedded in backgrounds from hydro events, as described in Sec. II C. Each of the five NNs listed in Table I were trained on this data set. The approximate importance of each parameter in each NN is visualized in Fig. A.3, which displays the feature importances using training random forest models trained with the same parameter lists. Some results from NN_{AllReco} are given in Figures 3-4. Fig. 3 reports the $p_{T,\text{jet}}^{\text{truth}}$ spectrum, the $p_{T,\text{jet}}^{\text{corr}}$ spectrum generated by correcting $p_{T,\text{jet}}^{\text{reco}}$ with NN_{AllReco} and also the $p_{T,\text{jet}}^{\text{corr}}$ spectra corrected using the AB method (without any NN).

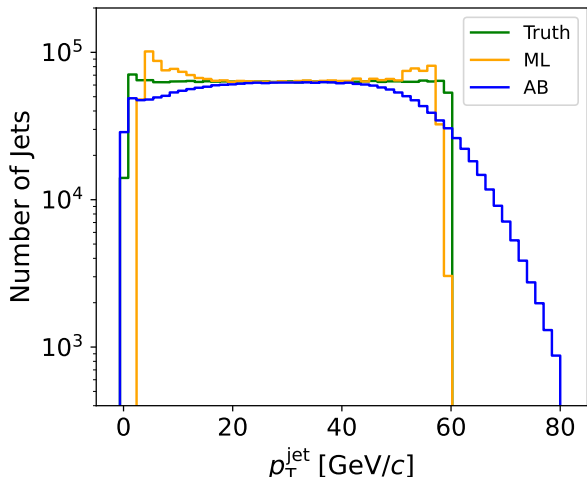


FIG. 3. Jet p_T distributions: truth jet, reco-jet corrected by the NN_{AllReco} neural network, and the reco-jet corrected using the AB method ($p_{T,\text{jet}}^{\text{corr}} \equiv p_{T,\text{jet}}^{\text{reco}} - \rho \times A$).

Note that when applying the AB method any jet with $p_{T,\text{jet}}^{\text{corr}} < 0$ GeV/c is discarded. This cut is commonly used in jet measurement analyses of real data. This results in the sharp boundary on the left hand side of the AB $p_{T,\text{jet}}^{\text{corr}}$ distribution in Fig. 3. There is no cut on jets used to train the neural network; however, the neural network itself learns that there are no training jets with $p_{T,\text{jet}}^{\text{truth}} \leq 0$ GeV/c or $p_{T,\text{jet}}^{\text{truth}} > 60$ GeV/c. As such, the ML $p_{T,\text{jet}}^{\text{corr}}$ distribution has a sharp cut at both the left-hand and right-hand side. This is to say, the ML has “learned” that any $p_{T,\text{jet}}^{\text{reco}}$ value close to 0 GeV/c cannot correspond to a truth jet sitting in an upward fluctuation in the bulk particle background; similarly any value close to 60 GeV/c cannot correspond to a truth jet in an downward fluctuation. This learned constraint is an artifact of the training data and has no corresponding truth in the physics of actual experimental data: a jet with $p_{T,\text{jet}}^{\text{reco}} \approx 60$ GeV/c could be the result of a higher $p_{T,\text{jet}}^{\text{truth}}$ jet sitting on a downward background fluctuation. However, in data the importance of downward fluctuations is suppressed by the steeply falling $p_{T,\text{jet}}^{\text{truth}}$ spectra.

Because the NNs learn the boundaries, the $\delta p_{T,\text{jet}}$ values near those boundaries are highly biased. To illustrate this effect, Fig. 4 shows the $\delta p_{T,\text{jet}}$ distributions for events with three ranges of $p_{T,\text{jet}}^{\text{truth}}$: one near each boundary and one in the middle. Note the “inward-tales” of the distributions near the boundary agree with the tails of the middle distribution, while their “outward” tales are truncated. The figure also reports the mean and standard deviation of each $\delta p_{T,\text{jet}}$ distribution. In Fig. 5 the mean and standard deviations of $\delta p_{T,\text{jet}}$ for a continuous set of ranges of $p_{T,\text{jet}}^{\text{truth}}$ are shown; markers show the mean $\delta p_{T,\text{jet}}$ values, and the error bars are scaled to equal the magnitude of the $\delta p_{T,\text{jet}}$ standard deviations. As is visually apparent, the neural network would introduce significant off-diagonal entries near the training boundaries in a correlation matrix of $p_{T,\text{jet}}^{\text{truth}}$ and $p_{T,\text{jet}}^{\text{corr}}$, whereas

the AB method, while having overall significantly larger distributions, would only do so for low- p_T jets.

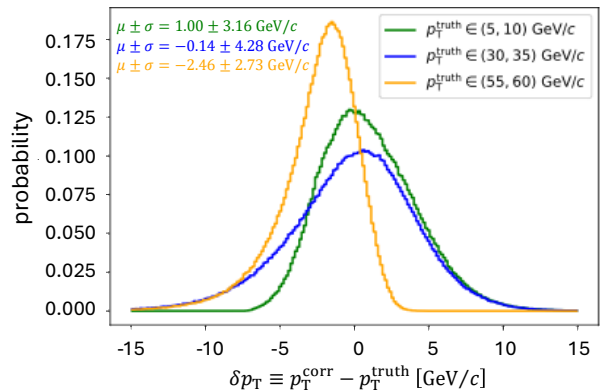


FIG. 4. The probability distribution of the residual error, $\delta p_{T,\text{jet}} \equiv p_{T,\text{jet}}^{\text{corr}} - p_{T,\text{jet}}^{\text{truth}}$, with $p_{T,\text{jet}}^{\text{corr}}$ from NN_{AllReco} for events with three ranges of $p_{T,\text{jet}}^{\text{truth}}$. Also listed are the mean and standard deviation of $\delta p_{T,\text{jet}}$ for each range.

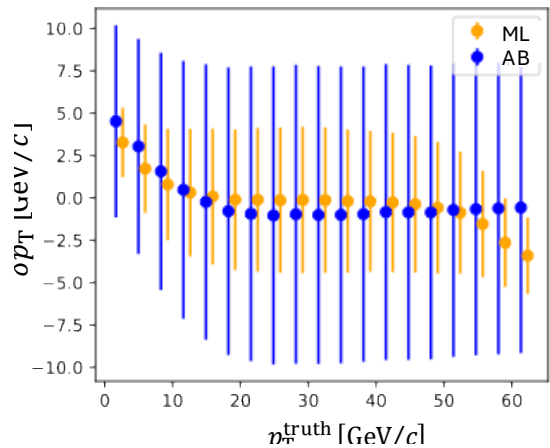


FIG. 5. The values of the mean (markers) and standard deviation (length of the attached vertical lines) of the $\delta p_{T,\text{jet}} \equiv p_{T,\text{jet}}^{\text{corr}} - p_{T,\text{jet}}^{\text{truth}}$ distributions for events with bins of $p_{T,\text{jet}}^{\text{truth}}$ (as indicated on the x -axis), with $p_{T,\text{jet}}^{\text{corr}}$ calculated by the area-based method and by NN_{AllReco} (refer to Table I). For visual clarity, the AB and ML markers are displayed with a small relative horizontal offset.

III. NEURAL NETWORK PERFORMANCE

A. Effects of Jet Quenching on $\delta p_{T,\text{jet}}$ from Neural Networks

Figure 6 shows the $\delta p_{T,\text{jet}}$ distributions from use of the five NNs listed in Table I in events with $\hat{p}_T \in [30, 31]$ of pp jets. The same results for four other ranges of \hat{p}_T are given in the appendix in Fig. A.4.

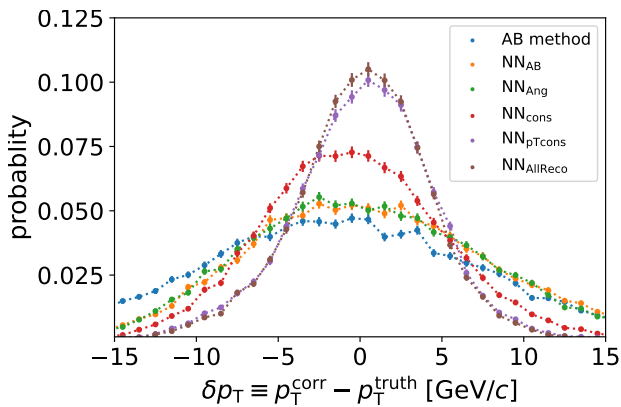


FIG. 6. The residual error distribution in neural network corrections from $p_{T,\text{jet}}^{\text{reco}}$ to $p_{T,\text{jet}}^{\text{corr}}$ for events generated with $\hat{p}_T \in [30, 31]$ GeV/c and trained on parameters listed in Table I.

When the NN background correction is performed on quenched jets, the $\delta p_{T,\text{jet}}$ distributions evolve with the magnitude of quenching. This evolution is shown in Fig. 7 for $\delta p_{T,\text{jet}}$ for jets in QGP bricks from 0 fm (no quenching) up to 8 fm using NN_{AllReco}. Comparable results for all the NNs, for five different selections of \hat{p}_T , are given in Figs A.5-A.9 in the appendix. Note that the biggest shift in $\delta p_{T,\text{jet}}$ occurs within the first two fm of quenching, which is within the range of quenching experienced by the jets in the hydro events and expected at RHIC energies.

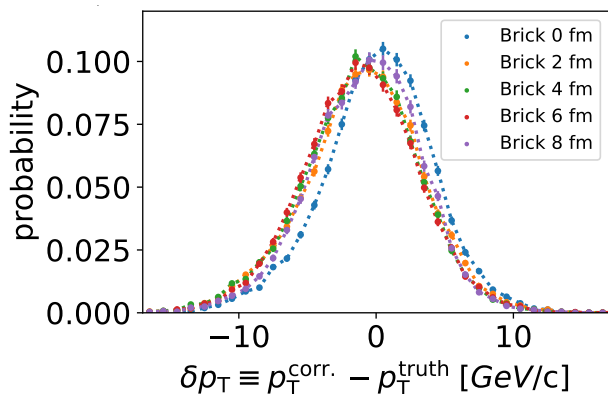


FIG. 7. The evolution of the distribution of $\delta p_{T,\text{jet}} \equiv p_{T,\text{jet}}^{\text{corr}} - p_{T,\text{jet}}^{\text{truth}}$ for jets undergoing quenching in different lengths of QGP (as listed) in which $p_{T,\text{jet}}^{\text{corr}}$ generated by NN_{AllReco} (refer to Table I) which was trained on jet events with no quenching. The events were generated with $\hat{p}_T \in [30, 31]$ GeV/c.

In order to compare the quenching effects between hydro and brick events, the mean ($\langle \delta p_{T,\text{jet}} \rangle$) and standard deviation ($\sigma(\delta p_{T,\text{jet}})$) of each $\delta p_{T,\text{jet}}$ distribution is reported for a series of brick lengths, along the values for hydro events. In the hydro events, the jet quenching path lengths are modeled individually in each event, and as such are not associated with a specific path length. Therefore, the hydro $\langle \delta p_{T,\text{jet}} \rangle$ and $\sigma(\delta p_{T,\text{jet}})$ values are

displayed as horizontal lines. These are shown in Fig.8 for jets at $\hat{p}_T \in [30, 31]$ GeV/c using NN_{AllReco}. The corresponding figures for the other four neural networks are given in the appendix in Fig. A.10 and Fig. A.11. In each case, the biases in $\delta p_{T,\text{jet}}$ for hydro events correspond to those in events using QGP bricks of 3 to 4 fm, which is consistent with the modification in jet fragmentation shown in Fig. 1, and confirms the choice of using quenching in 3.5 fm bricks of QGP as proxies for quenching in hydro events.

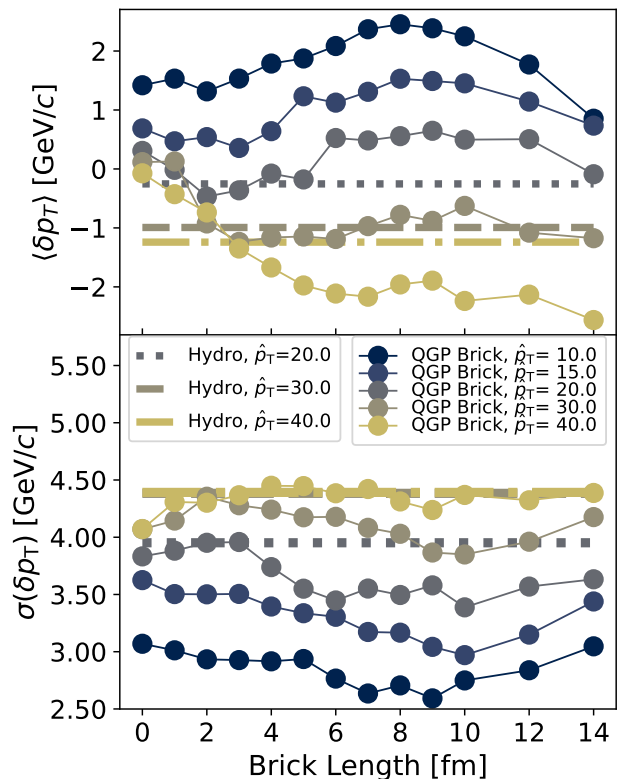


FIG. 8. The mean and standard deviation of the $\delta p_{T,\text{jet}} \equiv p_{T,\text{jet}}^{\text{corr}} - p_{T,\text{jet}}^{\text{truth}}$ distributions for $p_{T,\text{jet}}^{\text{corr}}$ generated from neural network NN_{AllReco} (trained with all parameters listed in Table I row (e)). Jets where quenched using a hydrodynamically simulated QGP, as well as bricks of QGP, and no quenching (at brick length of 0). The hydro data aren't associated with set QGP brick lengths, and are therefore displayed with horizontal lines located vertically at their $\langle \delta p_{T,\text{jet}} \rangle$ and $\sigma(\delta p_{T,\text{jet}})$ values.

B. Effects of $\delta p_{T,\text{jet}}$ Bias on Measuring $p_{T,\text{jet}}$

As seen in Fig. 8, using NNs for background corrections biases the resulting distributions of $\delta p_{T,\text{jet}}$. Of particular note, the biases are also jet- p_T dependent. In order to demonstrate the magnitude of effects these biases can result in actual measurements, we simulate a measurement of jet quenching using the NNs. The algorithm employed parallels the process used in actual detector jet measurements, and is simplified to focus on the jet background

rejection biases introduced by the mismatch in jet substructure between the quenched jets and those used to train the NNs. An outline of the methodology used in an actual experiment is given in Sec. III B 1, while the differences in this paper are listed in Sec. III B 2.

1. Algorithm to Measure Jets Quenching in Experiments

- a. Measured data consists of events with jets constituents clustered together with the heavy background resulting from heavy ion collisions. This clustering results in detector-level jets, with a spectrum of $p_{T,\text{jet}}^{\text{reco}}$ (i.e. $dp_{T,\text{jet}}^{\text{reco}}/dp_T$).
- b. The reco-jets are background corrected, commonly using the AB method, to jets with $p_{T,\text{jet}}^{\text{corr}}$.
- c. To determine the “truth-level” jets – i.e. the jets which would result if only the particle-level jet constituents were clusters – generate a correlation matrix correlating $p_{T,\text{jet}}^{\text{truth}}$ to distributions of $p_{T,\text{jet}}^{\text{corr}}$. To do this:
 - c.1 Use a MC generator to simulate pp jets (with corresponding values of $p_{T,\text{jet}}^{\text{truth}}$).
 - c.2 Propagate the pp jet constituents through a detailed physics simulation of the detector (e.g., [31]) to generate detector-level final state hadrons.
 - c.3 Separately, collect distributions of background hadrons from actual collision measurements. These are really just the measurements of evens with minimal trigger requirements.
 - c.4 Embed the detector-level hadrons of the pp jets into the actually measured backgrounds, and cluster into “reco-jets”.
 - c.5 Background correct the reco-jets into corr-jets using the same method as used in the measurement in step **b**.
 - c.6 Geometrically match the simulated pp jets (“truth jets”) to the corr-jets, using some cutoff in ΔR , $\left(\Delta R \equiv \sqrt{(\eta^{\text{truth}} - \eta^{\text{corr}})^2 + (\phi^{\text{truth}} - \phi^{\text{corr}})^2}\right)$. Fill pairs of matched jets into response matrix $\mathcal{M}(p_{T,\text{jet}}^{\text{truth}}, p_{T,\text{jet}}^{\text{reco}})$.
 - Unmatched pp jets are counted as “misses” and account for inefficiency in jet detection.
 - Unmatched reco-jets are “fakes” and account for jets resulting from clustering only the background.
- d. Use $\mathcal{M}(p_{T,\text{jet}}^{\text{truth}}, p_{T,\text{jet}}^{\text{reco}})$ along with the p_T spectra of the misses and fakes, to statistically correct the detector measured $p_{T,\text{jet}}^{\text{corr}}$ to the measured $p_{T,\text{jet}}^{\text{truth}}$.

- e. Scale the A+A events to an equivalent number of pp collisions. This is because hard partonic scatterings (jets) scale in a heavy ion collision by the number of equivalent nucleon-nucleon collisions; e.g., for hard scatterings, a head-on Au+Au collision is the equivalent of upwards of 1000 pp collisions. Report the “nuclear modification factor” R_{AA} , which is ratio of the scaled jet spectra to that in pp ; so named because if there is no jet quenching, then $R_{AA} \approx 1$.

2. Algorithm Used in this Paper to Measure Jets

The algorithm implemented for the results reported in this paper are comparable to that listed in Sec. III B 1. The differences listed below.

- a. The “measurement data” consists of JETSCAPE simulated jets quenched in 3.5 fm bricks of QGP which are embedded into background collected from the JETSCAPE hydro events. The following cuts are applied:
 - For the jets, use only jets from the highest- p_T IP collision.
 - If that IP has $|\eta| > 1$ discard the event.
 - Cluster the hadrons from this IP into anti- k_T the jet(s) with $R = 0.4$ jet using **FastJet** 3.4.2 [19].
 - Find the highest- p_T reconstructed jet within $\Delta R < 0.4$ of the IP, and label it as the “truth-jet”.
 - Embed the constituents of the truth-jet into the background hadrons from a hydro event, and re-cluster into “reco-jets”.
 - Find all reco-jets within $\Delta R \leq 0.3$ of the truth-jet, and save the highest- p_T jet as the reco-jet.

Herein, this process maps only the single “leading jet” from the highest- p_T IP. This is done for simplicity in the modeling. In an actual measurement (e.g., **a.**), of course, there is no knowledge what the underlying jet distribution is, and all jets per event would be recorded. As lower- p_T jets experience the effects of quenching more strongly, this method likely underestimates the final results of the effects of quenching.

- b. Same as **b.**, in which the background correction is conducted six times, once with the AB method and once with each of the five NNs (as listed in Tab. I). The results of all six methods are separately propagated through the following steps to individual results.

c. The steps to generate the $\mathcal{M}(p_{T,\text{jet}}^{\text{truth}}, p_{T,\text{jet}}^{\text{reco}})$ are identical to those in **c.1-c.6**, with the following specifics:

c.1 The embedded jets are the leading JETSCAPE pp jets, using the same cuts as in Step a.

c.2 Besides fiducial cuts in rapidity, $|\eta| \leq 1.0$ for IP and $|\eta| \leq 1.1$ for hadrons, the simulation does not account for detector effects. This is done to focus only on the effects of the NNs.

c.3 The background consist of the same body of hydro events as used in Step a.

c.4-c.6 Identical to Steps **c.4-c.6**.

d. The correction using $\mathcal{M}(p_{T,\text{jet}}^{\text{truth}}, p_{T,\text{jet}}^{\text{reco}})$ is done using an iterative Bayesian unfolding procedure implemented with the RooUnfold package [32], as is also used in actual measurements. Alternatively, the correction is also done by using single bin efficiencies (“1-Bin Eff.” in the result labels), in which the ratio of $p_{T,\text{jet}}^{\text{truth}}/p_{T,\text{jet}}^{\text{corr}}$ in the simulation is used as a single scaler multiplier to correct each p_T bin of the corrected jet spectra.

e. As this procedure is already scaled to only the leading jet generated per nucleon-nucleon collision (the quenched jets are generated as pp jets which are quenched in 3.5 fm bricks of plasma which are then embedded into backgrounds), then “ R_{AA}^{LeadJet} ” is defined directly as the ratio the measured jet spectra to a truth spectrum of leading truth jets in unquenched pp events.

IV. R_{AA}^{LeadJet} RESULTS

The algorithm detailed in Sec. III B 2 was used to calculate the corrected jet spectra for quenched jets using the AB method and all five NNs. The jet spectra for the unquenched jets (pp), truth-level quenched jets, and the “measurement” of the quench jet spectra are reported in Fig. 9, in which $\text{NN}_{\text{AllReco}}$ was used for the jet background correction. The R_{AA}^{LeadJet} values for both the real and the measured p_T ’s are also shown. The same information is shown for the other four NNs in the appendix in Fig. A.12 and Fig. A.13. For these jets – the lead jet only per event quenched in 3.5 fm bricks of QGP – the actual R_{AA}^{LeadJet} values, as estimated using bricks of QGP in simulation, are approximately independent at around 0.7 on jet p_T , while the error introduced by using the NN on quenched jets resulted in R_{AA}^{LeadJet} values up to 30% lower.

For comparison, the R_{AA}^{LeadJet} values resulting from using the AB method and all five NNs are shown together in Fig. 10. Notably, the AB method results in approximately the true value, as does NN_{AB} which is trained on the same parameters use in the AB method. All the

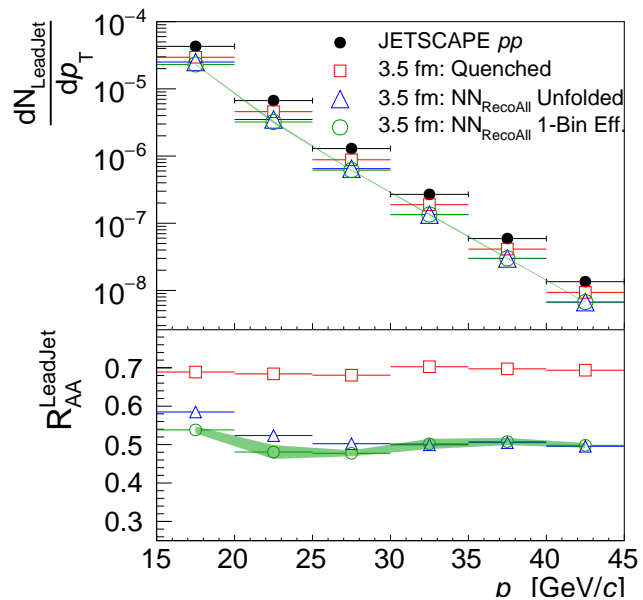


FIG. 9. Top panel: Spectra of the leading jet per event for pp (non-quenched) and quenched jets, counting only events with $p_{T,\text{jet}}^{\text{truth}} > 12$ GeV/c and $p_{T,\text{jet}}^{\text{reco}} - A_{\text{jet}}\rho_{\text{bkg}} > 0$ GeV/c, in addition to the measured spectra of quenched jets which are background corrected using the $\text{NN}_{\text{reco all}}$ and unfolded using both the single-bin efficiency (“1-Bin Eff.”) or Bayesian unfolding with 4 iterations (“Unfolded”). Bottom panel, the R_{AA} of the actual quenched spectra and the measured quenched spectra. The shaded area (which is quite narrow in the top panel) represents the uncertainty introduced by instability in the unfolding. Statistical errors are smaller than the plotting markers.

other NNs result in systematically lower R_{AA}^{LeadJet} values. Perhaps not surprisingly, R_{AA}^{LeadJet} generated with NN_{Ang} is the least biased out of these four NNs. If a jet undergoes partonic energy loss, and the jet clustering recovers (partly) the medium induced gluon emissions, then the impact on the angularity training parameter $\sum_i p_{T,i} \Delta R_i$ is mitigated. On the other hand, quenching increases the number of constituents monotonically and the corresponding bias in R_{AA}^{LeadJet} from NN_{Ncons} is the largest.

V. SUMMARY AND CONCLUSIONS

Models can be trained using substructure of jets clustered together with background particles from heavy ion collisions – in addition to the median background p_T density – to correct for the background component of the jet p_T , and result in considerably smaller residual errors than just subtracting the mean background in each event. However, in events with quenching, jet substructures are modified, which in turn biases the background corrections. This report studies those biases using best-in-class simulations from JETSCAPE to generate hydrodynamically modeled QGP, with resulting background particle distributions, and associated jet quenching in Au+Au

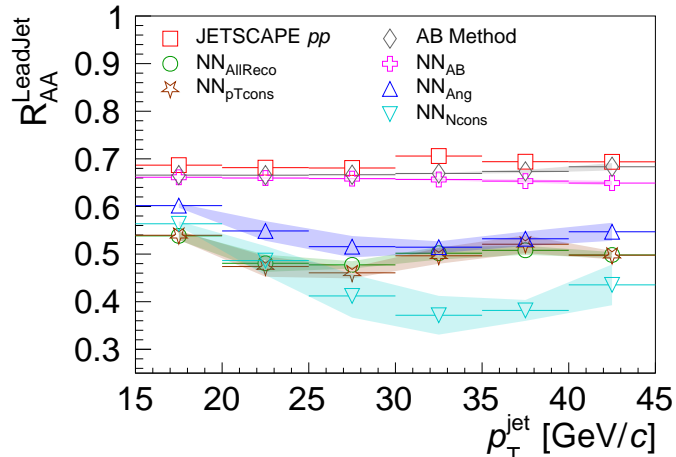


FIG. 10. The measured R_{AA} of the quenched jets, background corrected with the traditional AB Method ($p_{T,jet}^{reco} - A_{jet}\rho_{bkg}$) and five neural networks, trained on parameters listed in Table I. The actual ratio of the quenched jets to unquenched jets is also shown. Note that in this context, the spectra are only of the leading jet in each event, counting only events with the jet with $p_{T,jet}^{truth} > 12$ GeV/c and $p_{T,jet}^{reco} - A_{jet}\rho_{bkg} > 12$ GeV/c. The shaded areas account for the instability in the unfolding. Statistical errors are smaller than the markers.

collisions at $\sqrt{s_{NN}} = 200$ GeV. It should be noted, however, that jet-medium interactions are not captured in the simulations used.

We trained NNs on using a variety of jet substructure parameters using pp jets embedded into the realistic heavy ion backgrounds, and reported the biases through the residual errors on background correction on quenched jets. The biases are observed to be significant. They are also dependent on jet- p_T , which is qualitatively different from those from AB background corrections which are independent of jet substructure whose resolution is limited by the inhomogeneity in the background density.

In order to demonstrate the possible magnitude of the error introduced by these biases, we mimic as closely as possible an actual jet R_{AA} measurement using the NNs for background p_T corrections. In order to make these measurements, we compared quenching in computationally cheaper “bricks” of QGP, and found that bricks 3.5 fm thick are a good proxy for quenching in collisions with hydrodynamically modeled QGP at RHIC energies. Accordingly, we simulated the R_{AA} measurement using jets quenched in these bricks of QGP and embedded into the backgrounds from the “hydro” events. The resulting error propagated in the R_{AA} are significant, up to a maximum of around 47% when using NN_{Ncons} , and no less than 18% for any p_T range for any NN. The only exception is NN_{AB} which is trained only on the parameters used in the AB method, and therefore independent of jet substructure.

Any application of background correction using jet fragmentation must presuppose an amount of jet quenching in order to then proceed to actually measure the jet

quenching. It may be possible to parameterize the biases and determine bounding errors as has been done at LHC energies; see, e.g. [24]. If, when such a procedure is used, it is not apparent which among the outcomes are the most probable, we strongly recommend the results be reported as a bounded range without any markers. Alternatively, it may also yet prove possible to use an iterative method to appropriately select and refine the value of the modeled quenching with the measurement of jets themselves.

Alternative to training NNs directly on the jet substructure, with the inherent uncertainties introduced by jet quenching, it may be possible to use ML to distinguish between jet-like objects which are clustered purely from background particles (i.e. “fake jets”) and those containing real jet constituents. There is an essentially unbounded supply of background measurements available at each detector, and perhaps ML could become very sensitive to the presence of “some signal” in this background without being selectively sensitive to the type (or substructure) of that signal. If achievable, such a classifier could dramatically decrease the abundance of fake jets to real jets in measurements. In turn, this could facilitate jet measurements down to lower- p_T ranges than currently accessible as RHIC energies.

ACKNOWLEDGMENTS

This work was supported by the U.S. Department of Energy Office of Science, Office of Nuclear Physics under Award No. DE-FG02-92ER40713. The authors would like to thank Hannah Bossi, Helen Caines, and Raymond James for insightful discussions on machine learning in jet physics, and Chun Shen for discussion and expertise in JETScape.

Appendix A: Additional Figures

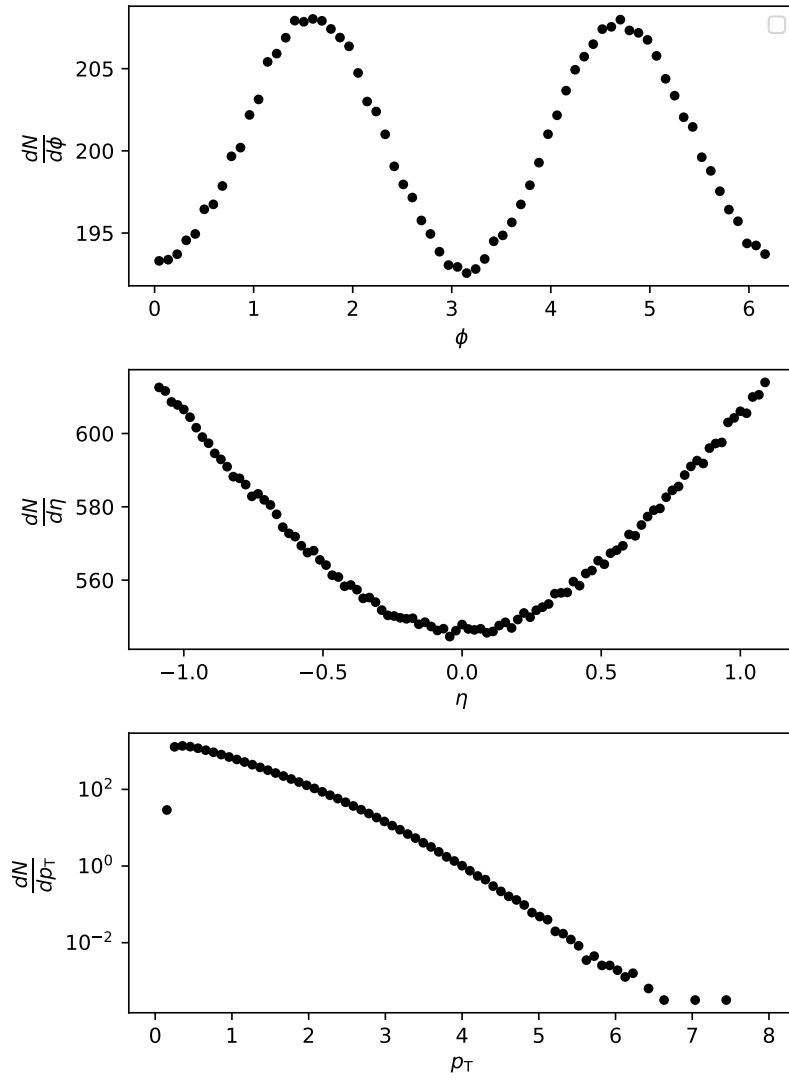


FIG. A.1. Distributions of ϕ , η , and p_T densities of background particles, averaged over all background events. The v^2 flow shown is a result of JETSCAPE aligning all impact parameters along the x -axis.

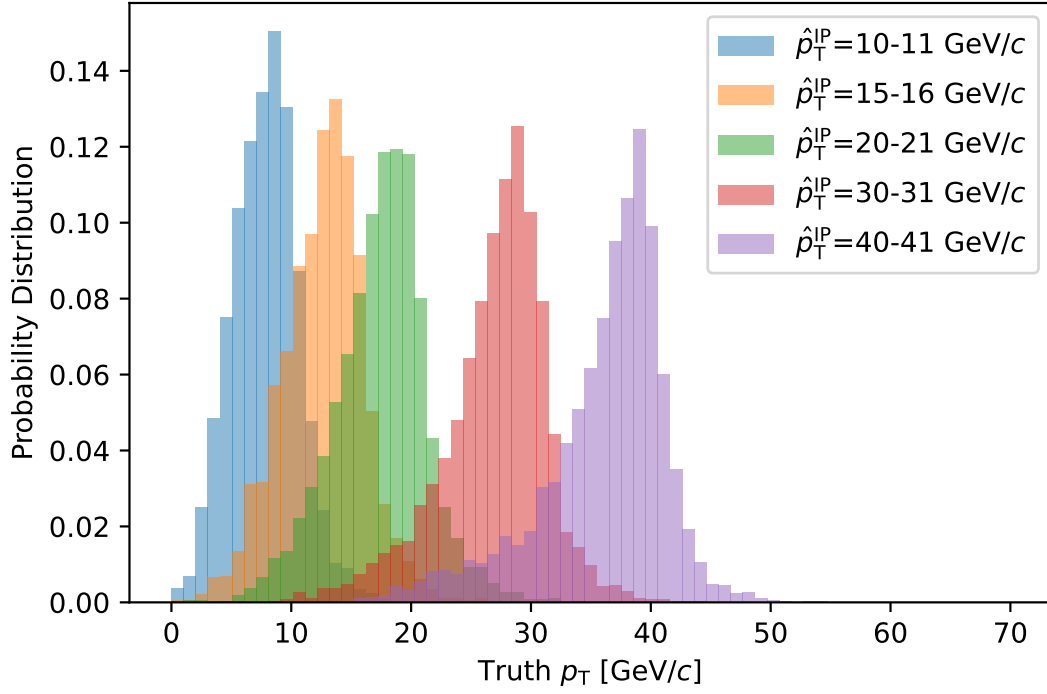


FIG. A.2. Distribution of $p_{T,\text{jet}}^{\text{truth}}$ per JETSCAPE \hat{p}_T parameter selection for the non-quenched datasets.

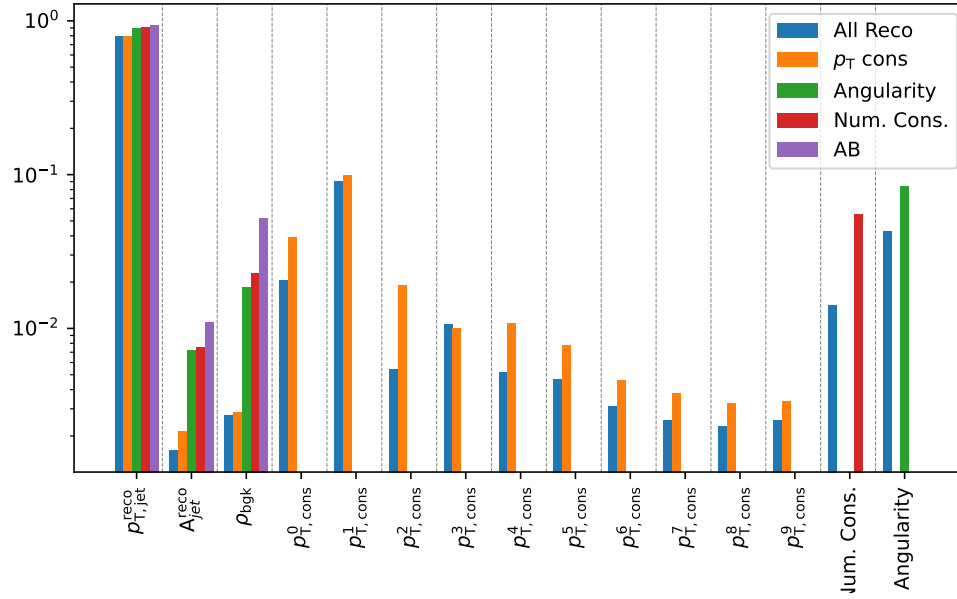


FIG. A.3. Random forest feature importances, using random forests trained on the sets of parameters (listed in Table I) which were used to train the Neural Networks. These are consistent with those reported in prior publication [23].

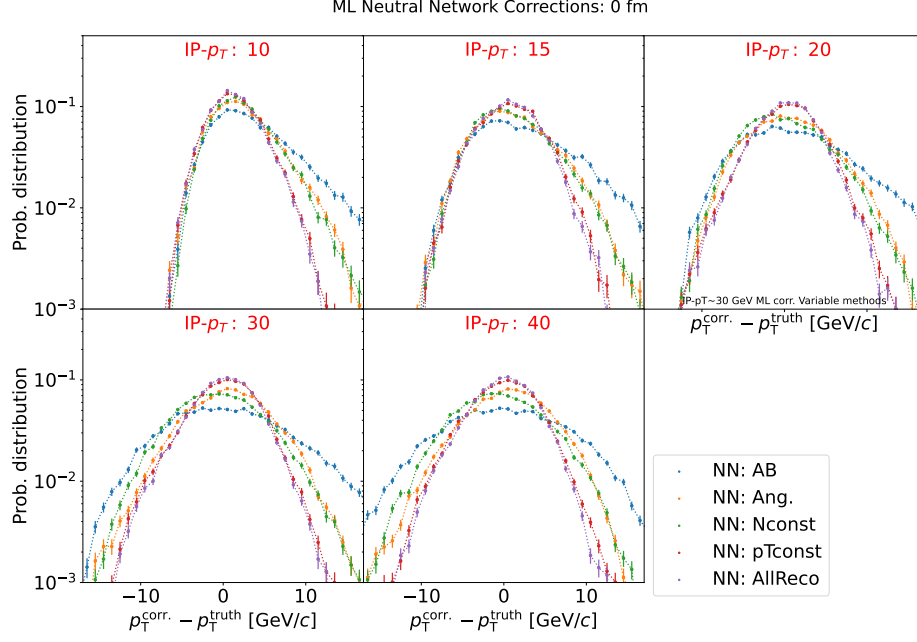


FIG. A.4. The distributions of $\delta p_{T,jet} \equiv p_{T,jet}^{corr} - p_{T,jet}^{truth}$ for distributions in neural network corrections from $p_{T,jet}^{reco}$ to $p_{T,jet}^{corr}$ for events generated with five ranges of \hat{p}_T and trained on parameters listed in Table I.

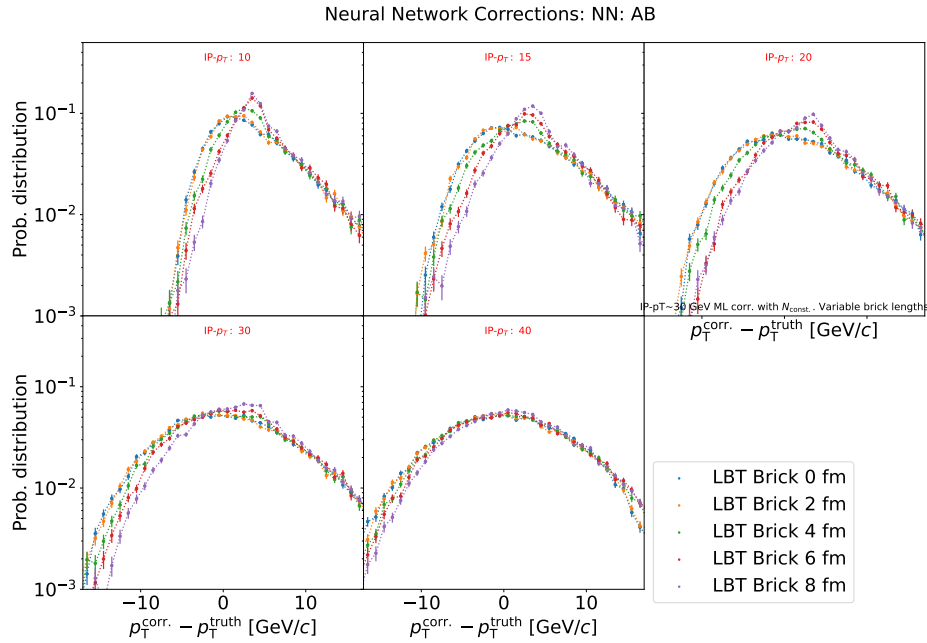


FIG. A.5. Distributions of $\delta p_{T,jet} \equiv p_{T,jet}^{corr} - p_{T,jet}^{truth}$ for distributions with correction made by a neural network trained on ρ_{bkg} , $p_{T,jet}^{truth}$, $p_{T,jet}^{reco}$, and A_{jet} . Within each panel, the evolution of $\delta p_{T,jet}$ for events with no quenching to quenching with a 8 fm brick of QGP.

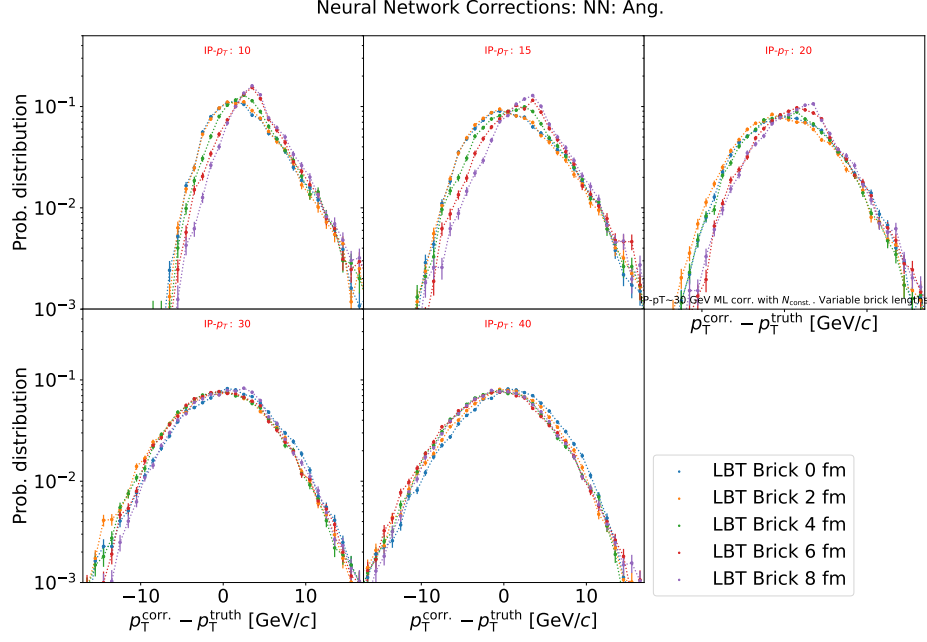


FIG. A.6. Distributions of $\delta p_{T,\text{jet}} \equiv p_{T,\text{jet}}^{\text{corr}} - p_{T,\text{jet}}^{\text{truth}}$ for distributions with correction made by a neural network trained on ρ_{bkg} , $p_{T,\text{jet}}^{\text{truth}}$, $p_{T,\text{jet}}^{\text{truth}}$, A_{jet} , and jet angularity. Within each panel, the evolution of $\delta p_{T,\text{jet}}$ for events with no quenching to quenching with a 8 fm brick of QGP.

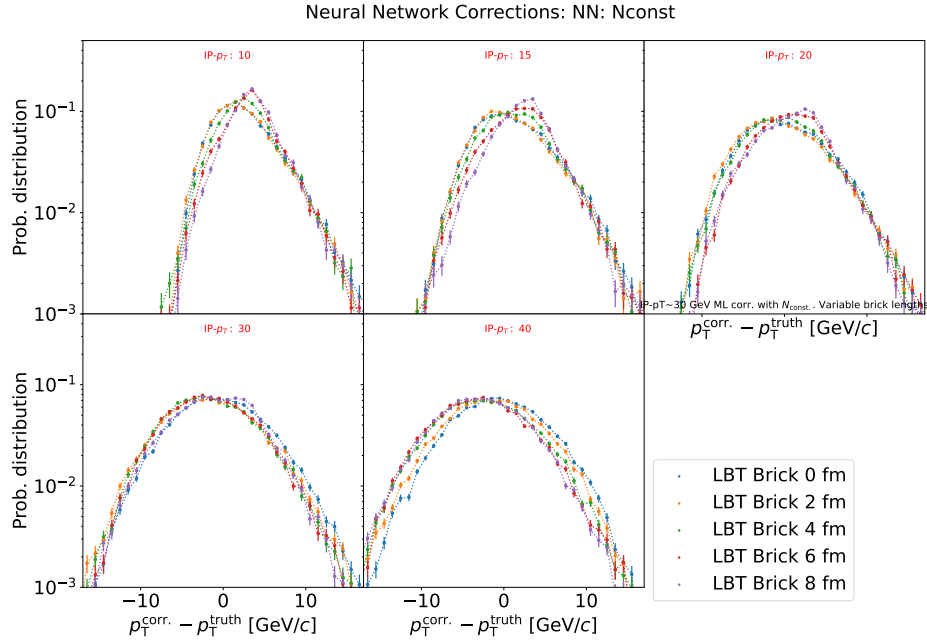


FIG. A.7. Distributions of $\delta p_{T,\text{jet}} \equiv p_{T,\text{jet}}^{\text{corr}} - p_{T,\text{jet}}^{\text{truth}}$ for distributions with correction made by a neural network trained on ρ_{bkg} , $p_{T,\text{jet}}^{\text{truth}}$, $p_{T,\text{jet}}^{\text{truth}}$, A_{jet} , and the number of jet constituents. Within each panel, the evolution of $\delta p_{T,\text{jet}}$ for events with no quenching to quenching with a 8 fm brick of QGP.

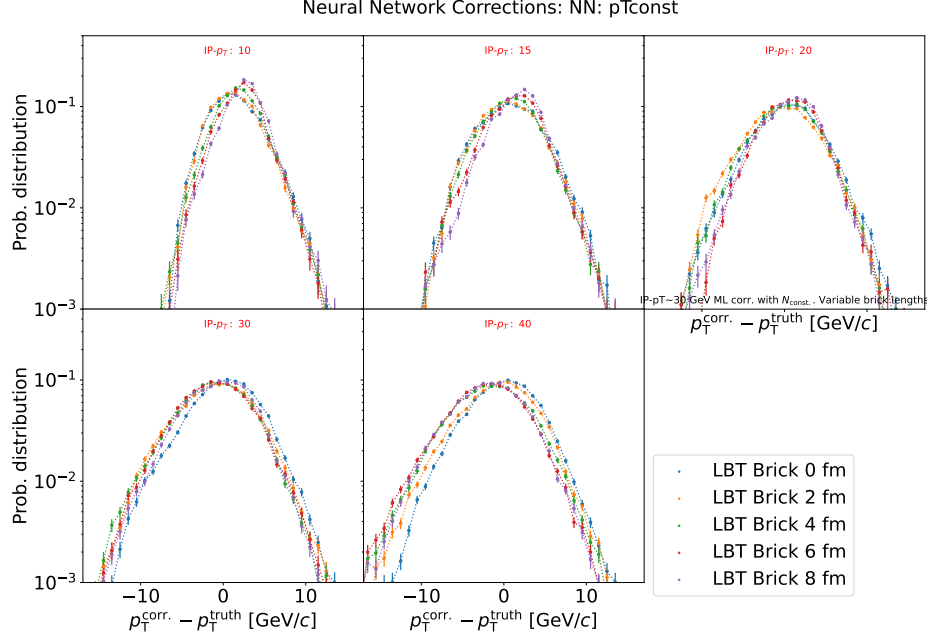


FIG. A.8. Distributions of $\delta p_{T,\text{jet}} \equiv p_{T,\text{jet}}^{\text{corr}} - p_{T,\text{jet}}^{\text{truth}}$ for distributions with correction made by a neural network trained on ρ_{bkg} , $p_{T,\text{jet}}^{\text{truth}}$, $p_{T,\text{jet}}$, A_{jet} , the p_T of the leading 10 jet constituents. Within each panel, the evolution of $\delta p_{T,\text{jet}}$ for events with no quenching to quenching with a 8 fm brick of QGP.

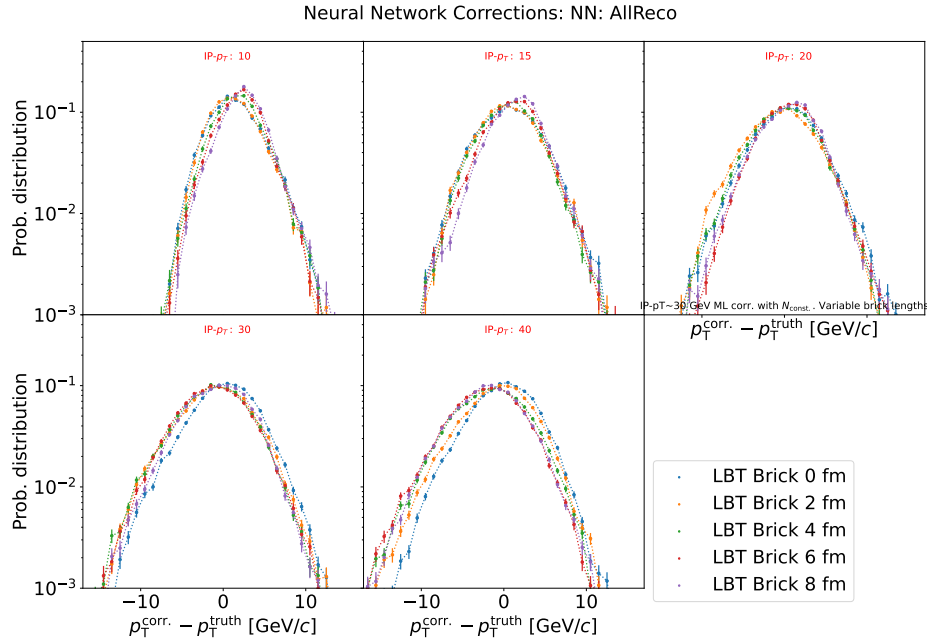


FIG. A.9. Distributions of $\delta p_{T,\text{jet}} \equiv p_{T,\text{jet}}^{\text{corr}} - p_{T,\text{jet}}^{\text{truth}}$ for distributions with correction made by a neural network trained on ρ_{bkg} , $p_{T,\text{jet}}^{\text{truth}}$, $p_{T,\text{jet}}$, A_{jet} , jet angularity, the number of jet constituents, and the p_T of the leading 10 jet constituents. Within each panel, the evolution of $\delta p_{T,\text{jet}}$ for events with no quenching to quenching with a 8 fm brick of QGP.

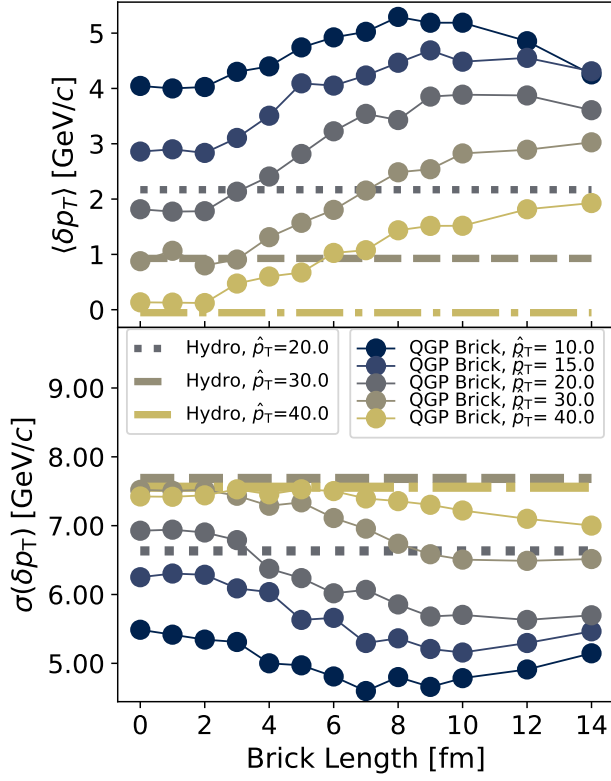
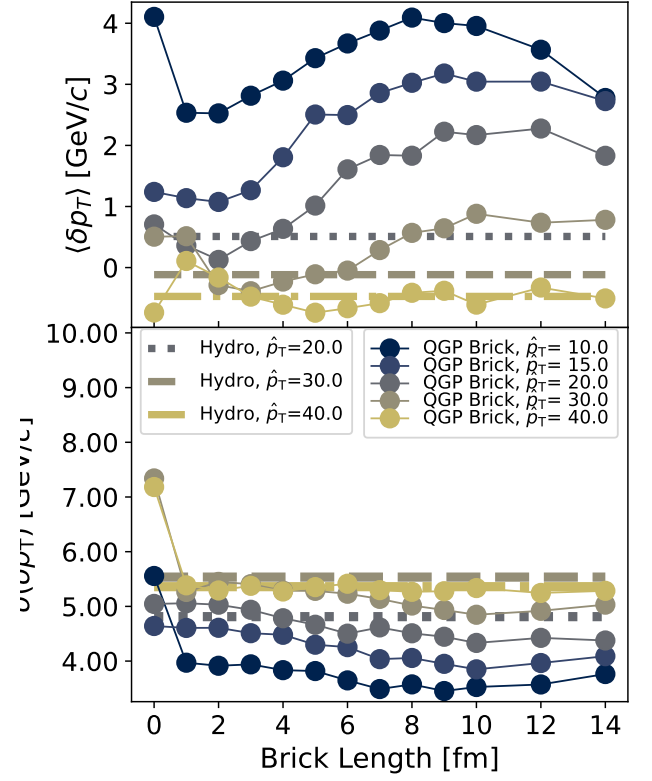
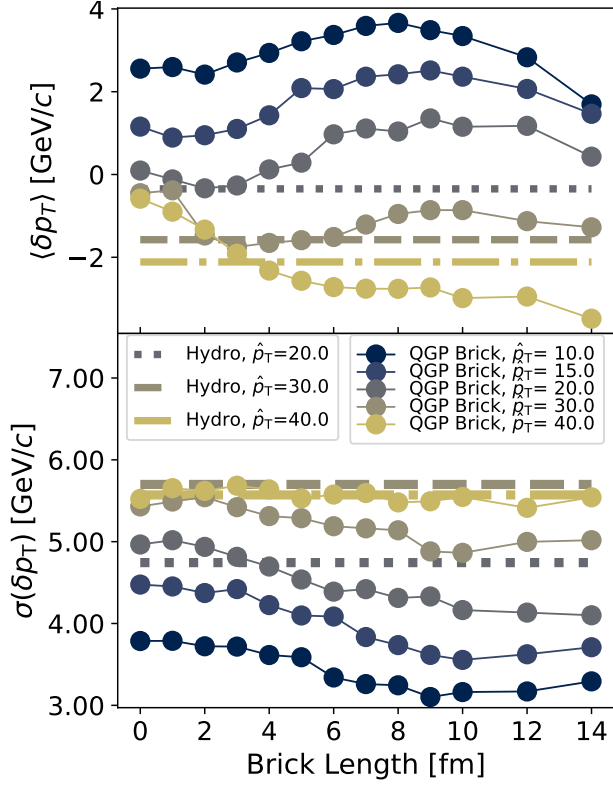
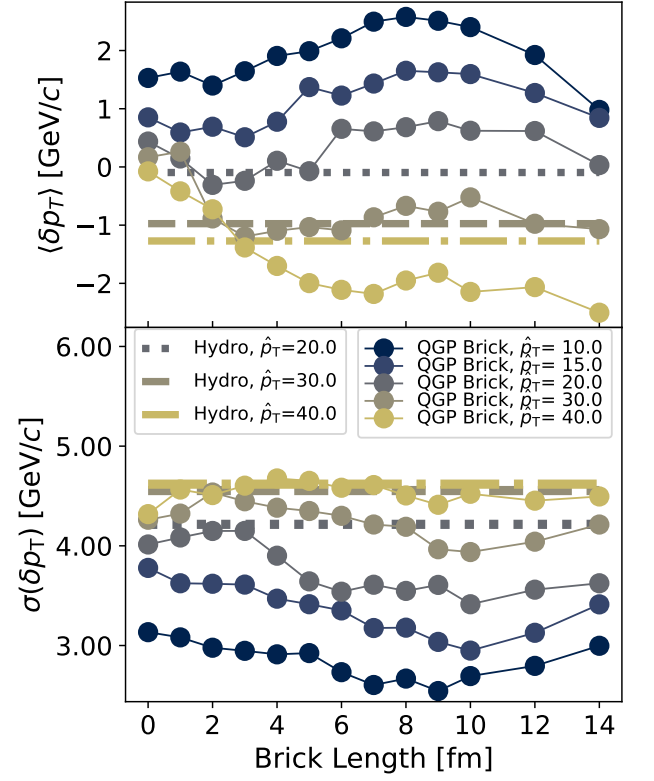
(a) Neural network trained with ρ_{bkg} , A_{jet} , $p_{T,\text{jet}}^{\text{truth}}$, and $p_{T,\text{jet}}^{\text{reco}}$ (b) Neural network trained with ρ_{bkg} , A_{jet} , $p_{T,\text{jet}}^{\text{truth}}$, $p_{T,\text{jet}}^{\text{reco}}$, and jet angularity

FIG. A.10. Mean and standard deviations of the $\delta p_{T,\text{jet}} \equiv p_{T,\text{jet}}^{\text{corr}} - p_{T,\text{jet}}^{\text{truth}}$ distributions for $p_{T,\text{jet}}^{\text{corr}}$ generated from a neural network trained on jet events with no quenching using all parameters listed in in Table I (i.e. row (e)). The jets corrected are generated using hydrodynamic simulated QGP, as well as bricks of QGP, and (for “Brick Length=0”) no quenching. The hydro data aren’t associated with set brick lengths, and are displayed with horizontal lines at their $\langle \delta p_{T,\text{jet}} \rangle$ and $\sigma(\delta p_{T,\text{jet}})$ values.

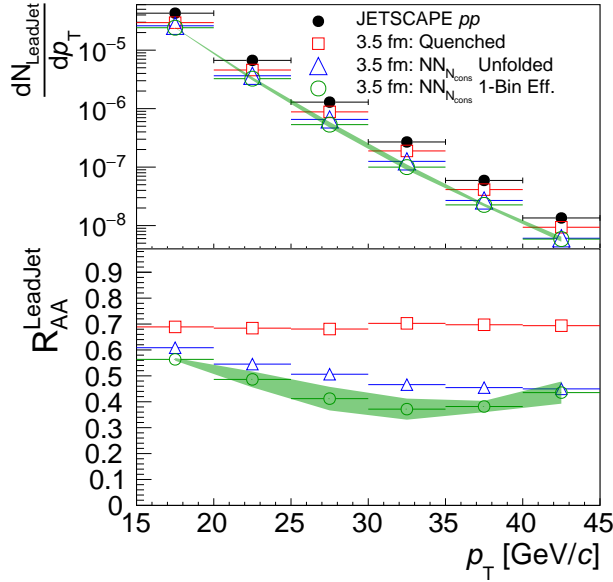


(a) Neural network trained with ρ_{bkg} , A_{jet} , $p_{T,\text{jet}}^{\text{truth}}$, $p_{T,\text{jet}}^{\text{reco}}$, and number of jet constituents

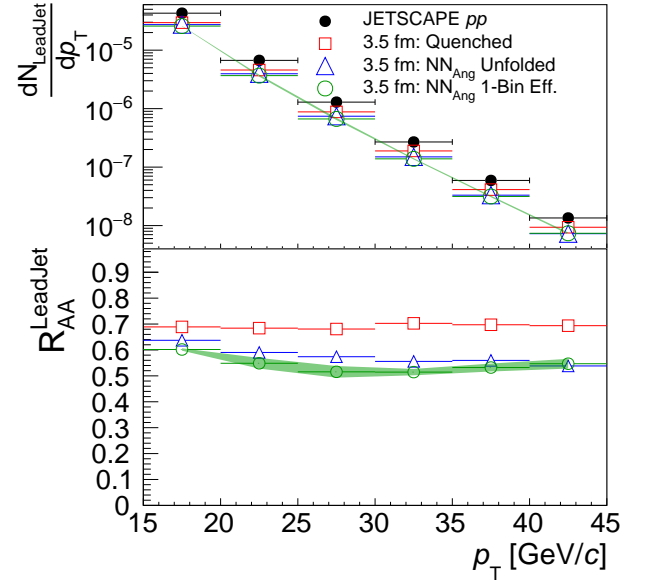


(b) Neural network trained with ρ_{bkg} , A_{jet} , $p_{T,\text{jet}}^{\text{truth}}$, $p_{T,\text{jet}}^{\text{reco}}$, and p_T of the jet's ten highest- p_T constituents

FIG. A.11. Mean and standard deviations of the $\delta p_{T,\text{jet}} \equiv p_{T,\text{jet}}^{\text{corr}} - p_{T,\text{jet}}^{\text{truth}}$ distributions for $p_{T,\text{jet}}^{\text{corr}}$ generated from a neural network trained on jet events with no quenching using all parameters listed in in Table I (i.e. row (e)). The jets corrected are generated using hydrodynamic simulated QGP, as well as bricks of QGP, and (for “Brick Length=0”) no quenching. The hydro data aren't associated with set brick lengths, and are displayed with horizontal lines at their $\langle \delta p_{T,\text{jet}} \rangle$ and $\sigma(\delta p_{T,\text{jet}})$ values.

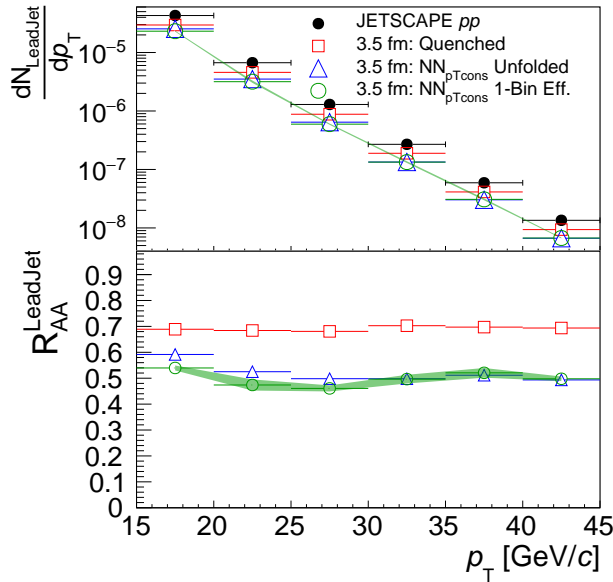


(a) Using neural network NN_{Ncons} , which is trained with ρ_{bkg} , A_{jet} , $p_{T,jet}^{truth}$, $p_{T,jet}^{reco}$, and number of jet constituents.

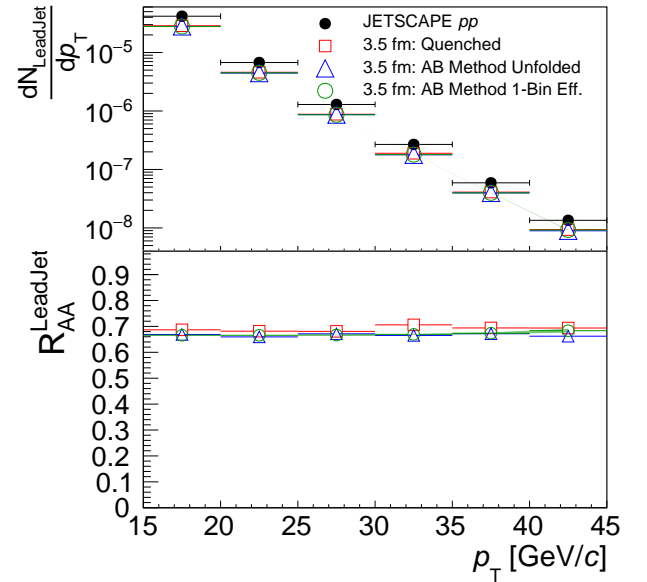


(b) Using neural network NN_{Ang} , which is trained with ρ_{bkg} , A_{jet} , $p_{T,jet}^{truth}$, $p_{T,jet}^{reco}$, and the jet angularity.

FIG. A.12. Jet spectra unquenched, quenched in 3.5 fm of QGP, and the measured quenched jet spectra corrected for background using Neural network's with the parameters listed. (Training parameters are also listed in Table. I.



(a) Using neural network NN_{Ncons} , which is trained with ρ_{bkg} , A_{jet} , $p_{T,jet}^{truth}$, $p_{T,jet}^{reco}$, and the p_T of highest 10 p_T jet constituents.



(b) Using neural network NN_{Ang} , which is trained with ρ_{bkg} , A_{jet} , $p_{T,jet}^{truth}$, $p_{T,jet}^{reco}$.

FIG. A.13. Jet spectra unquenched, quenched in 3.5 fm of QGP, and the measured quenched jet spectra corrected for background using Neural network's with the parameters listed. (Training parameters are also listed in Table. I.

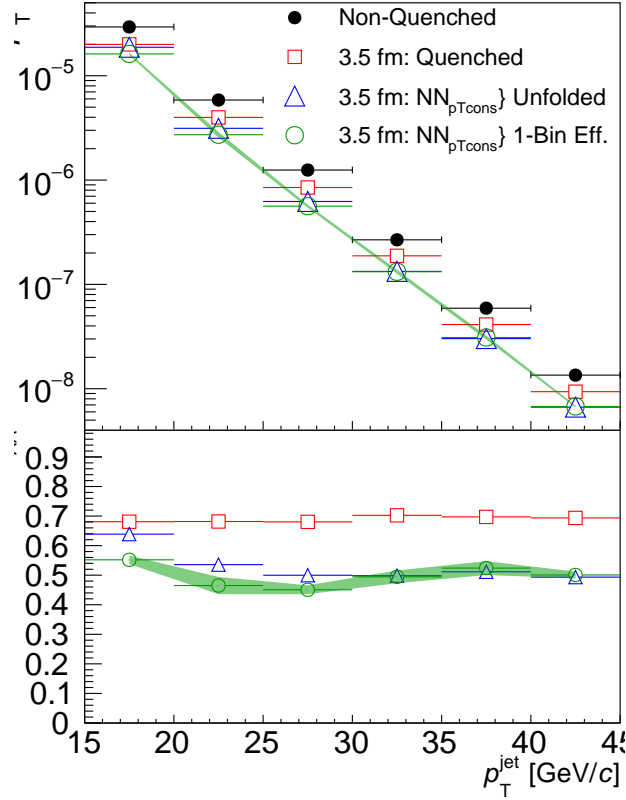


FIG. A.14. Jet spectra unquenched, quenched in 3.5 fm of QGP, and the measured quenched jet spectra corrected for background using neural network NN_{pTcons} , which is trained with ρ_{bkg} , A_{jet} , $p_{T,jet}^{truth}$, $p_{T,jet}^{reco}$, and p_T of the jet's ten highest- p_T constituents.

Appendix B: Hardware and Software

1. Hardware

All code was run on a single machine equipped with an AMD Ryzen Threadripper 3960X Processor, two NVIDIA GeForce RTX 3090 GPUs, and 128 GB of DDR4 ram.

2. Software

The following software process was used. Input files, scripts, and codes, are archived at [github.site](https://github.com).

- JETSCAPE 3.6.4 [26] was pulled from online at <https://github.com/JETSCAPE/JETSCAPE>, compiled locally, and run with XML files.
- JETSCAPE's output `.dat.gz` files were converted into ROOT [33] files via a Python script.
- A locally compiled C++ code, using ROOT 6.28/10 [33] and FastJet 3.4.2 [19] libraries, was used to cluster and match jets, calculated ρ_{bkg} , etc... The output files were ROOT files.
- Python scripts and Jupyter Notebooks were used to process the output files and run the machine learning. The principle Python libraries used are:
 - Python 3.10.12
 - Pandas 2.2.1

- Scikit-learn 0.23.2 [34]
- NumPy 1.26.4
- Pickle 4.0
- json 2.0.9
- TensorFlow 2.13.1 [30]
- PyArrow 15.0.1

-
- [1] J. W. Harris and B. Muller, *Ann. Rev. Nucl. Part. Sci.* **46**, 71 (1996), arXiv:hep-ph/9602235.
 - [2] I. Arsene *et al.* (BRAHMS), *Nucl. Phys. A* **757**, 1 (2005), arXiv:nucl-ex/0410020.
 - [3] B. B. Back *et al.* (PHOBOS), *Nucl. Phys. A* **757**, 28 (2005), arXiv:nucl-ex/0410022.
 - [4] J. Adams *et al.* (STAR), *Nucl. Phys. A* **757**, 102 (2005), arXiv:nucl-ex/0501009.
 - [5] K. Adcox *et al.* (PHENIX), *Nucl. Phys. A* **757**, 184 (2005), arXiv:nucl-ex/0410003.
 - [6] G. Aad *et al.* (ATLAS), *Phys. Rev. Lett.* **105**, 252303 (2010), arXiv:1011.6182 [hep-ex].
 - [7] S. Chatrchyan *et al.* (CMS), *Phys. Rev. C* **84**, 024906 (2011), arXiv:1102.1957 [nucl-ex].
 - [8] K. Aamodt *et al.* (ALICE), *Phys. Rev. Lett.* **105**, 252302 (2010), arXiv:1011.3914 [nucl-ex].
 - [9] T. Niida and Y. Miake, *AAPPS Bull.* **31**, 12 (2021), arXiv:2104.11406 [nucl-ex].
 - [10] R. Baier, *Nucl. Phys. A* **715**, 209 (2003), arXiv:hep-ph/0209038.
 - [11] J. Adams *et al.* (STAR), *Phys. Rev. Lett.* **93**, 252301 (2004), arXiv:nucl-ex/0407007.
 - [12] R. Brock *et al.* (CTEQ), *Rev. Mod. Phys.* **67**, 157 (1995).
 - [13] L. Cunqueiro and A. M. Sickles, *Prog. Part. Nucl. Phys.* **124**, 103940 (2022), arXiv:2110.14490 [nucl-ex].
 - [14] N. J. Abdulameer *et al.* (PHENIX), (2024), arXiv:2408.11144 [hep-ex].
 - [15] M. Abdulhamid *et al.* (STAR), *Phys. Rev. C* **109**, 044909 (2024), arXiv:2307.13891 [nucl-ex].
 - [16] M. Abdulhamid *et al.* (STAR), *Phys. Rev. C* **110**, 044908 (2024), arXiv:2404.08784 [nucl-ex].
 - [17] M. Cacciari, G. P. Salam, and G. Soyez, *JHEP* **04**, 063, arXiv:0802.1189 [hep-ph].
 - [18] M. Cacciari and G. P. Salam, *Phys. Lett. B* **659**, 119 (2008), arXiv:0707.1378 [hep-ph].
 - [19] M. Cacciari, G. P. Salam, and G. Soyez, *Eur. Phys. J. C* **72**, 1896 (2012), arXiv:1111.6097 [hep-ph].
 - [20] T. Sjöstrand, *Computer Physics Communications* **246**, 106910 (2020).
 - [21] C. Bierlich *et al.*, *SciPost Phys. Codeb.* **2022**, 8 (2022), arXiv:2203.11601 [hep-ph].
 - [22] J. Bellm *et al.*, *Eur. Phys. J. C* **76**, 196 (2016), arXiv:1512.01178 [hep-ph].
 - [23] R. Haake and C. Loizides, *Phys. Rev. C* **99**, 064904 (2019), arXiv:1810.06324 [nucl-ex].
 - [24] S. Acharya *et al.* (ALICE), *Phys. Lett. B* **849**, 138412 (2024), arXiv:2303.00592 [nucl-ex].
 - [25] T. Mengel, P. Steffanic, C. Hughes, A. C. O. Da Silva, and C. Nattrass, (2024), arXiv:2402.10945 [hep-ex].
 - [26] J. H. Putschke *et al.*, (2019), arXiv:1903.07706 [nucl-th].
 - [27] D. Everett *et al.* (JETSCAPE), *Phys. Rev. C* **103**, 054904 (2021), arXiv:2011.01430 [hep-ph].
 - [28] A. Kumar *et al.* (JETSCAPE), *Phys. Rev. C* **107**, 034911 (2023), arXiv:2204.01163 [hep-ph].
 - [29] S. D. Ellis and D. E. Soper, *Phys. Rev. D* **48**, 3160 (1993), arXiv:hep-ph/9305266.
 - [30] M. Abadi *et al.*, (2016), arXiv:1603.04467 [cs.DC].
 - [31] S. Agostinelli *et al.* (GEANT4), *Nucl. Instrum. Meth. A* **506**, 250 (2003).
 - [32] T. Adye, in *PHYSTAT 2011* (CERN, Geneva, 2011) pp. 313–318, arXiv:1105.1160 [physics.data-an].
 - [33] R. Brun, F. Rademakers, and S. Panacek, in *CERN School of Computing (CSC 2000)* (2000) pp. 11–42.
 - [34] F. Pedregosa *et al.*, *J. Machine Learning Res.* **12**, 2825 (2011), arXiv:1201.0490 [cs.LG].